

# MEMS segmented-based adaptive optics scanning laser ophthalmoscope

Silvestre Manzanera,<sup>1,\*</sup> Michael A. Helmbrecht,<sup>2</sup> Carl J. Kempf,<sup>2</sup> and Austin Roorda<sup>1</sup>

<sup>1</sup>University of California, Berkeley, Berkeley, CA 94720. USA

<sup>2</sup>Iris AO, Inc., Berkeley, CA, USA

\*silmanro@berkeley.edu

**Abstract:** The performance of a MEMS (micro-electro-mechanical-system) segmented deformable mirror was evaluated in an adaptive optics (AO) scanning laser ophthalmoscope. The tested AO mirror (Iris AO, Inc, Berkeley, CA) is composed of 37 hexagonal segments that allow piston/tip/tilt motion up to 5  $\mu\text{m}$  stroke and  $\pm 5$  mrad angle over a 3.5 mm optical aperture. The control system that implements the closed-loop operation employs a 1:1 matched 37-lenslet Shack-Hartmann wavefront sensor whose measurements are used to apply modal corrections to the deformable mirror. After a preliminary evaluation of the AO mirror optical performance, retinal images from 4 normal subjects over a  $0.9^\circ \times 0.9^\circ$  field size were acquired through a 6.4 mm ocular pupil, showing resolved retinal features at the cellular level. Cone photoreceptors were observed as close as 0.25 degrees from the foveal center. In general, the quality of these images is comparable to that obtained using deformable mirrors based on different technologies.

©2011 Optical Society of America

**OCIS codes:** (330.4460) Ophthalmic optics and devices; (110.1080) Active or adaptive optics.

---

## References and links

1. R. H. Webb, G. W. Hughes, and O. Pomerantzeff, "Flying spot TV ophthalmoscope," *Appl. Opt.* **19**(17), 2991–2997 (1980).
2. R. H. Webb and G. W. Hughes, "Scanning laser ophthalmoscope," *IEEE Trans. Biomed. Eng.* **BME-28**(7), 488–492 (1981).
3. R. H. Webb, G. W. Hughes, and F. C. Delori, "Confocal scanning laser ophthalmoscope," *Appl. Opt.* **26**(8), 1492–1499 (1987).
4. A. Roorda, F. Romero-Borja, W. Donnelly Iii, H. Queener, T. J. Hebert, and M. C. W. Campbell, "Adaptive optics scanning laser ophthalmoscopy," *Opt. Express* **10**(9), 405–412 (2002).
5. F. Romero-Borja, K. Venkateswaran, A. Roorda, and T. Hebert, "Optical slicing of human retinal tissue in vivo with the adaptive optics scanning laser ophthalmoscope," *Appl. Opt.* **44**(19), 4032–4040 (2005).
6. K. Venkateswaran, A. Roorda, and F. Romero-Borja, "Theoretical modeling and evaluation of the axial resolution of the adaptive optics scanning laser ophthalmoscope," *J. Biomed. Opt.* **9**(1), 132–138 (2004).
7. H. W. Babcock, "The possibility of compensating astronomical seeing," *Publ. Astron. Soc. Pac.* **65**(386), 229–236 (1953).
8. F. Roddier, *Adaptive Optics in Astronomy* (Cambridge University Press, 1999).
9. R. Tyson, *Principles of Adaptive Optics* (CRC Press, 2010).
10. H. Hofer, L. Chen, G. Y. Yoon, B. Singer, Y. Yamauchi, and D. R. Williams, "Improvement in retinal image quality with dynamic correction of the eye's aberrations," *Opt. Express* **8**(11), 631–643 (2001).
11. E. J. Fernández, P. M. Prieto, and P. Artal, "Wave-aberration control with a liquid crystal on silicon (LCOS) spatial phase modulator," *Opt. Express* **17**(13), 11013–11025 (2009).
12. P. Prieto, E. Fernández, S. Manzanera, and P. Artal, "Adaptive optics with a programmable phase modulator: applications in the human eye," *Opt. Express* **12**(17), 4059–4071 (2004).
13. F. Vargas-Martín, P. M. Prieto, and P. Artal, "Correction of the aberrations in the human eye with a liquid-crystal spatial light modulator: limits to performance," *J. Opt. Soc. Am. A* **15**(9), 2552–2562 (1998).
14. J. Z. Liang, D. R. Williams, and D. T. Miller, "Supernormal vision and high-resolution retinal imaging through adaptive optics," *J. Opt. Soc. Am. A* **14**(11), 2884–2892 (1997).
15. E. J. Fernández, I. Iglesias, and P. Artal, "Closed-loop adaptive optics in the human eye," *Opt. Lett.* **26**(10), 746–748 (2001).
16. M. Glanc, E. Gendron, F. Lacombe, D. Lafaille, J. F. Le Gargasson, and P. Lena, "Towards wide-field retinal imaging with adaptive optics," *Opt. Commun.* **230**(4-6), 225–238 (2004).

17. E. Dalimier and C. Dainty, "Comparative analysis of deformable mirrors for ocular adaptive optics," *Opt. Express* **13**(11), 4275–4285 (2005).
18. N. Doble, G. Yoon, L. Chen, P. Bierden, B. Singer, S. Olivier, and D. R. Williams, "Use of a microelectromechanical mirror for adaptive optics in the human eye," *Opt. Lett.* **27**(17), 1537–1539 (2002).
19. Y. H. Zhang, S. Poonja, and A. Roorda, "MEMS-based adaptive optics scanning laser ophthalmoscopy," *Opt. Lett.* **31**(9), 1268–1270 (2006).
20. B. Hulburd and D. Sandler, "Segmented mirrors for atmospheric compensation," *Opt. Eng.* **29**(10), 1186–1190 (1990).
21. D. S. Acton and R. C. Smithson, "Solar imaging with a segmented adaptive mirror," *Appl. Opt.* **31**(16), 3161–3169 (1992).
22. M. C. Roggemann, V. M. Bright, B. M. Welsh, S. R. Hick, P. C. Roberts, W. D. Cowan, and J. H. Comtois, "Use of micro-electro-mechanical deformable mirrors to control aberrations in optical systems: theoretical and experimental results," *Opt. Eng.* **36**(5), 1326–1338 (1997).
23. W. D. Cowan, M. K. Lee, B. M. Welsh, V. M. Bright, and M. C. Roggemann, "Surface micromachined segmented mirrors for adaptive optics," *IEEE J. Sel. Top. Quantum Electron.* **5**(1), 90–101 (1999).
24. A. Tuantranont and V. M. Bright, "Segmented silicon-micromachined microelectromechanical deformable mirrors for adaptive optics," *IEEE J. Sel. Top. Quantum Electron.* **8**(1), 33–45 (2002).
25. D. J. Dagle, W. D. Cowan, O. B. Spahn, G. D. Grossetete, A. J. Grine, M. J. Shaw, P. J. Resnick, and B. Jokiel, "Large-stroke MEMS deformable mirrors for adaptive optics," *J. Microelectromech. Syst.* **15**(3), 572–583 (2006).
26. N. Doble, D. T. Miller, G. Yoon, and D. R. Williams, "Requirements for discrete actuator and segmented wavefront correctors for aberration compensation in two large populations of human eyes," *Appl. Opt.* **46**(20), 4501–4514 (2007).
27. J. J. Hunter, B. Masella, A. Dubra, R. Sharma, L. Yin, W. H. Merigan, G. Palczewska, K. Palczewski, and D. R. Williams, "Images of photoreceptors in living primate eyes using adaptive optics two-photon ophthalmoscopy," *Biomed. Opt. Express* **2**(1), 139–148 (2011).
28. J. I. W. Morgan, J. J. Hunter, W. H. Merigan, and D. R. Williams, "The reduction of retinal autofluorescence caused by light exposure," *Invest. Ophthalmol. Vis. Sci.* **50**(12), 6015–6022 (2009).
29. E. A. Rossi, M. Chung, A. Dubra, J. J. Hunter, W. H. Merigan, and D. R. Williams, "Imaging retinal mosaics in the living eye," *Eye (Lond.)* **25**(3), 301–308 (2011).
30. D. Miller, L. Thibos, and X. Hong, "Requirements for segmented correctors for diffraction-limited performance in the human eye," *Opt. Express* **13**(1), 275–289 (2005).
31. M. A. Helmbrecht, M. He, T. Juneau, M. Hart, and N. Doble, "Segmented MEMS deformable-mirror for wavefront correction," *Proc. SPIE* **6376**, 63760D, 63760D-9 (2006).
32. J. W. Oliver, G. Pocock, R. Vincelette, S. Kumru, G. D. Noojin, K. J. Schuster, D. Stolarski, A. Shingledecker, and B. A. Rockwell, "In vivo investigation of near infrared retinal lesions utilizing two adaptive optics enhanced imaging modalities," *Proc. SPIE* **7175**, 71750H, 71750H-9 (2009).
33. N. Doble, C. Kempf, M. Helmbrecht, and A. Roorda, "Closed loop adaptive optics in the human eye using a segmented MEMS deformable mirror," *Invest. Ophthalmol. Vis. Sci.* **49**, ARVO E-Abstract 4195 (2008).
34. N. Doble, and S. Choi, "Widefield imaging of the human retina using adaptive optics," *Invest. Ophthalmol. Vis. Sci.* **50**, ARVO E-Abstract 1062 (2009).
35. T. Wilson, "The role of the pinhole in confocal imaging systems," in *The Handbook of Biological Confocal Microscopy*, J. B. Pawley, ed. (Plenum, New York, 1990), pp. 99–113.
36. S. A. Burns, R. Tumber, A. E. Elsner, D. Ferguson, and D. X. Hammer, "Large-field-of-view, modular, stabilized, adaptive-optics-based scanning laser ophthalmoscopy," *J. Opt. Soc. Am. A* **24**(5), 1313–1326 (2007).
37. K. Grieve, P. Tiruveedhula, Y. H. Zhang, and A. Roorda, "Multi-wavelength imaging with the adaptive optics scanning laser ophthalmoscopy," *Opt. Express* **14**(25), 12230–12242 (2006).
38. M. A. Helmbrecht and T. Juneau, "Piston-tip-tilt positioning of a segmented MEMS deformable mirror," *Proc. SPIE* **6467**, 64670M, (2007).
39. C. R. Vogel, D. W. Arathorn, A. Roorda, and A. Parker, "Retinal motion estimation in adaptive optics scanning laser ophthalmoscopy," *Opt. Express* **14**(2), 487–497 (2006).
40. J. Porter, A. Guirao, I. G. Cox, and D. R. Williams, "Monochromatic aberrations of the human eye in a large population," *J. Opt. Soc. Am. A* **18**(8), 1793–1803 (2001).

---

## 1. Introduction

In the early 1980s, Webb et al. [1,2] devised a new ophthalmoscope to image the living human retina. This instrument, called the confocal scanning laser ophthalmoscope (SLO), was based on a confocal optical imaging system and a scanning laser light beam illuminating the retina. It was shown to provide higher image contrast and light efficiency than conventional imaging systems [3].

But, as in any other ophthalmoscope, the objective lens of the imaging system is the eye's optical system comprised of the cornea and crystalline lens, which are affected by optical aberrations that degrade the quality of the retinal images. In order to solve this problem, adaptive optics (AO) was incorporated in the SLO. The new instrument, the adaptive optics

scanning laser ophthalmoscope (AOSLO) [4] allowed visualization of the living human retina at cellular level with improved lateral and axial resolution [5,6].

AO is a technique that has proven to be effective in improving the resolution of ground-based telescope images [7–9] and correcting the eye's aberrations to obtain enhanced in vivo retinal images [10]. Briefly, an AO system consists of two elements, a wavefront sensor (WFS) that measures the aberrations and a corrector that removes the wavefront error. Significant efforts have been made to build and test these correcting devices. Some of them are based on the optical properties of liquid crystals [11–13] and others, the most widely used, are deformable mirrors (DM) that make use of different types of technologies to modify the shape of a mirror surface [14–17]. Among these, AO mirrors based on MEMS (micro-electro-mechanical-systems) technology have proved to be especially well suited for applications in the eye [18], due to their reduced size, and capability of fine spatial control of the wavefront. Making use of these advantages, Zhang et al. [19] built a compact AOSLO suitable for a clinical environment.

In all of the aforementioned studies, the DMs employed were of the continuous face sheet type. That is, the mirror surface employs a single reflecting deformable layer. But the problem of shaping a reflecting surface can also be tackled using an array of tiled flat mirrors, so-called segmented mirrors, whose facets can be driven independently to shape the wavefront. Initially, bulky segmented mirrors were built for astronomical applications. In 1990 Hulburd and colleagues [20] described and characterized a 512-segment, 22-cm diameter segmented mirror. And in 1992 [21] a 19-segment hexagonally packed mirror, 2.8-cm across each segment, was used to image the Sun.

MEMS technology allowed the manufacture of segmented mirrors with much reduced sizes. In 1997, the first experimental demonstration of aberration correction using a MEMS hexagonal piston micromirror array was reported [22]. Since then, a number of other studies have characterized other piston-only [23,24] and piston-tip-tilt [25] segmented mirrors. In general, although these devices showed to be good aberration correctors they also showed poor optical efficiency. The reasons for the latter were the big spaces between segments or reduced fill factor and the poor flatness of the segments, both which caused light losses and diffraction effects. Although some effort was made to overcome this problem by using a lenslet array in front of the mirror to focus light on the segments, other technical issues arose [22,24].

Why would one choose to use segmented mirrors for vision applications? Segmented mirrors do not offer immediate optical benefits over more conventional DM technology [26]. Nor do they represent a path toward a less expensive device compared to other MEMS technologies. In some respects, the 37-segment mirror used in this report represents a step backward in terms of optical control. By comparison, the Boston Micromachines deformable mirror, which is currently used in our laboratory, has similar stroke with 140 actuators behind a continuous face-sheet reflector. Nevertheless, segmented mirrors offer some unique advantages for future AO applications for vision science. For example, segmented mirrors are more scalable than continuous face-sheet designs. Each actuator is independent, so there are no new optical constraints imposed by adding more elements. Second, there is more flexibility for coatings on the segmented reflectors. Advanced coatings may prove useful for specific imaging applications like 2-photon [27] or autofluorescence [28] where light efficiency is paramount. Finally, the ability to tip and tilt actuators can be used to deflect regions of the pupil out of the optical path, offering an efficient and effective way to control the pupil aperture. Pupil control can be used to limit pupil size and shape, or can be used to bypass scattering caused by small cataracts or highly aberrated regions arising from keratoconus or other disorders. None of these applications are implemented in this paper, because our first interest was in assessing the basic performance of a segmented mirror in a modern AOSLO design. In our opinion, the performance of a system depends as much on the optical design of the instrument as on the quality of wavefront sensor and corrector. Given the evolution and proven benefits of careful optical design for ophthalmic AO systems [29], it's worth reassessing alternate DM technology in such a modern design. If a 37-element segmented

mirror design works reasonably well, then the prospects are good for better performance with a MEMS segmented DM that has higher actuator counts.

In order to make these devices useful for vision applications, as pointed out by some authors [26,30], the fill factor should be well above 90%. In the last years, a new generation of MEMS segmented mirrors [31] that have a 98% fill factor, flatten below 7-nm rms (for some models) and have very flat segments (3-20 nm rms, depending on model) have become available (Iris AO, Inc., Berkeley, CA).

Recently, an Iris AO mirror was used in an AO retinal imaging system to explore retinal lesions in primates after infrared radiation overexposure [32]. In the human eye, after confirming its capabilities as a wavefront corrector [33] it was used in a flood illuminated fundus camera [34]. But, to date, the performance of MEMS segmented mirrors in an AOSLO for high resolution retinal imaging in the living human eye has not been tested yet. In the present work, an Iris AO 37-segment mirror was used as the corrector element in an AOSLO and its performance was evaluated.

## 2. Methods

### 2.1. The AOSLO

The DM is integrated into the AOSLO as depicted in Fig. 1. The light delivery (LD) module, through a beam splitter, introduces an 840 nm (50-nm bandwidth) collimated beam in the optical system, reaching the eye after reflecting off the DM, the horizontal scanner (HS) and the vertical scanner (VS). The infrared light comes from a superluminescent diode (Broadlighter S840, Superlum, Russia). The HS and the VS are a resonant scanner and a

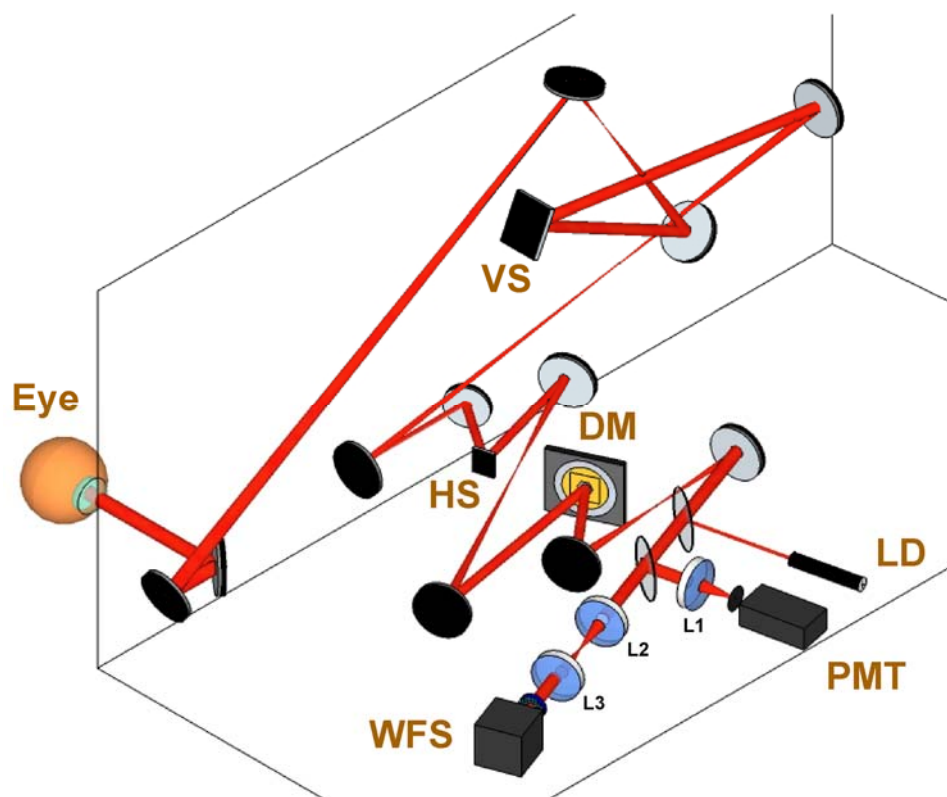


Fig. 1. Schematic diagram of the AOSLO setup. LD: light delivery; PMT: photomultiplier tube; WFS: wavefront sensor; DM: deformable mirror; HS: horizontal scanner; VS: vertical scanner. The optical setup is built along two perpendicular planes to remove astigmatism.

galvanometric scanner, respectively, manufactured by Electro-Optics Products Corp, Flushing Meadows, NY. The resonant scanner works at 16 kHz producing a sinusoidal scan that is coupled to the galvanometric scanner which generates a sawtooth pattern at 1/525th of the fast scan frequency. The diffusely reflected light from each point of the drawn raster scan on the retina transmits inversely along the ingoing path. Part of this light is then reflected on a beam splitter, focused on a pinhole by means of a collecting lens (L1) and finally detected by a GaAs photo multiplier tube (PMT) (Hamamatsu, Japan). The ideal pinhole diameter is around 20  $\mu\text{m}$  [35] although a 80- $\mu\text{m}$  pinhole was finally chosen to increase throughput. Dedicated software, an electronic module and a frame grabbing board (GenesisLC, Matrox, Canada) convert the detected signal by the PMT into an image of the retina. The rest of light reflected off the retina is used to measure the wavefront error and feed the AO control system that corrects for the aberrations of the eye.

Pairs of spherical mirrors forming 4f systems assure that the eye's pupil, the VS, the HS and the DM planes are optically conjugated. Finally, to relay the wavefront onto the lenslet array in the WFS two achromatic doublets (L2, L3) are used, yielding a 1:1 magnification between the DM and the WFS, as required. The mirror focal lengths are chosen in such a way that the whole aperture of the DM, 3.5 mm, is used to correct a 6.4 mm pupil in the eye. Three flat mirrors fold the path to meet the space and system design requirements.

One of the most important requirements was to remove, in the eye's pupil plane, the residual astigmatism induced by off-axis reflections from the spherical mirrors. To achieve this goal, equal amounts of astigmatism was generated along two perpendicular planes, parallel and perpendicular to the optical table [3,36]. The combination left only defocus at the eye's pupil, which could be removed by simple axial displacement of the mirrors. An optimization procedure was carried out using optical design software (Zemax<sup>®</sup>, Bellevue, WA) to determine the angles of incidence of the light on each mirror necessary to yield a diffraction limited system over a 1.6°x1.6° field of view with minimum raster scan distortion.

Most of the components used in this system, including light delivery, detection, scanners and detection, were the same that were previously utilized in AOSLOs described in earlier work. This means that a meaningful comparison can be made between the current and previous system's performance [4,37].

## 2.2. The AO mirror

The AO mirror is a MEMS segmented mirror manufactured by Iris AO, Inc. (Berkeley, CA), model PTT111-5 with a 7.0-nm RMS flatness. Each of the 37 hexagonal segments that constitute the array is driven by three actuators that allow piston/tip/tilt motion up to 5- $\mu\text{m}$  stroke and  $\pm 5$  mrad angle. The segments are tightly packed to achieve a 98% fill factor over a 3.5-mm optical aperture. Figure 2 shows a general view of the AO mirror and a schematic diagram of the segment arrangement.

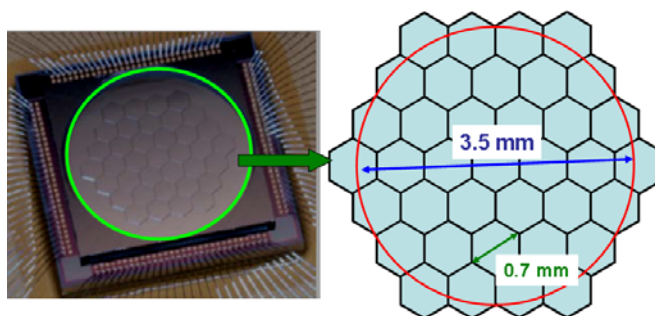


Fig. 2. Image of the Iris AO mirror and a detailed view of the hexagonal segment arrangement. The optical aperture is 3.5 mm and each facet is 0.7 mm from vertex to vertex. Courtesy of Iris AO, Inc.

The reflecting surface is attached to an actuator platform that is elevated above the substrate by three flexures. The flexures provide mechanical restoring forces that counter the attractive electrostatic forces of the three underlying diamond-shaped electrodes. Equal voltages on each of the electrodes cause the segment to be pulled downward in a piston motion whereas different voltage distributions produce tip and tilt motions. An illustrative diagram of the latter can be seen in Fig. 3. These movements are not independent and an excessive use of one of them compromises the ability to actuate the others. In order to allow push-pull motions an initial voltage is applied to every segment to put them in a bias position.

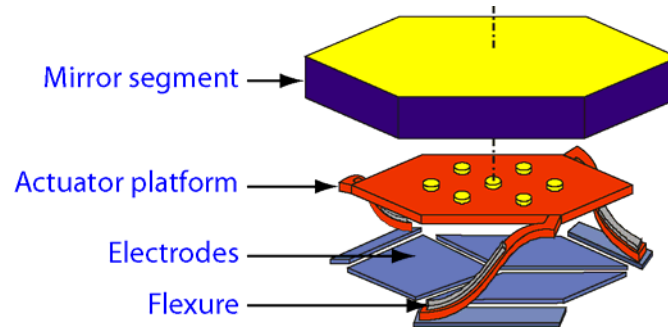


Fig. 3. Schematic diagram of the structure underlying each mirror segment that allows its different motions. The mirror segment is attached to an actuator platform that can be pushed and tilted by applying the necessary voltage distribution to a set of three electrodes. The flexures provide mechanical restoring forces that counter the attractive electrostatic forces. Courtesy of Iris AO, Inc.

### 2.3. The AO system

Iris AO provided, along with the DM, an AO control system that included the DM electronic driver, a Shack-Hartmann WFS and the control software to implement closed-loop AO control. The lenslet array in the WFS comprised microlenses on a hexagonal pattern matching the pitch of the DM segments. The optics relaying the DM onto the lenslet array plane yielded a 1:1 magnification and the DM and WFS were aligned so that the deviations of each segment were sensed only by one lenslet. The intrinsic decoupling of the DM segments together with this particular WFS configuration could potentially have enabled zonal wavefront corrections. However, considering that a Shack-Hartmann WFS is not able to measure piston, a zonal correction might create abrupt steps between segments and produce undesired diffraction effects. For this reason, a modal approach - fitting the mirror segments to the continuous surface expressed by a set of Zernike polynomials - was adopted. The DMs supplied by Iris AO were factory calibrated to enable precision open-loop positioning to better than 30 nm RMS over the majority of the operating space [38]. This was important in order to apply modal corrections while keeping the segments co-phased to a high degree.

The camera used in the WFS was a UP-680CL manufactured by Uniq Vision Inc, (Santa Clara, CA). It was connected to a frame grabber board in the control PC via a camera link interface. The acquired images were processed at 60 Hz to obtain the spot locations using a simple center of gravity algorithm.

Additional software settings were also included, providing a greater flexibility in the closed-loop operation, that allowed the operator to select both the maximum number of Zernike polynomial orders that were used to correct for the measured wavefront and the sensing region that was used to estimate the aberrations. The latter is useful in those cases where the outer spots from the WFS do not provide reliable estimations of the wavefront for their corresponding pupil locations and might affect the modal reconstruction for the whole pupil. In this case, an extrapolation of the measured wavefront is used to apply corrections to the AO mirror over the rest of the pupil.

### 3. Results

#### 3.1. Preliminary test on a model eye

Prior to using the AOSLO to obtain retinal images from human eyes, the quality of the AO correction was evaluated using a model eye, consisting of a lens that served as the refractive elements in the eye (cornea and crystalline lens) and a diffuse surface acting as the retina.

The first parameter selected to evaluate the quality of the AO correction is, usually, the residual RMS of the wavefront measured by the WFS. For the model eye with different amounts of induced defocus, the residual RMS was always below  $0.025\ \mu\text{m}$  through the 6.4 mm pupil. However, for this particular AO system, the RMS must not be considered alone in order to evaluate its performance. First, because the wavefront error is sampled with a limited number of lenslets, there could potentially be undetected high spatial frequency features in the wavefront. Secondly, the discontinuous nature of the AO mirror surface could induce diffractive effects, which affect the AOSLO image but are not detected by the WFS.

Hence, to overcome the aforementioned issues, the quality of the AO correction was evaluated through two measurements, the PSF provided by the AO mirror -which greatly determines the image resolution- and the double pass image (DPI) that is formed on the confocal pinhole in the AOSLO, which is the ultimate determination of the optical image quality.

##### 3.1.1. PSF evaluation

The PSF was obtained by illuminating the flat AO mirror with a 633-nm collimated laser beam and focusing the reflected light on a CCD camera. To achieve this while keeping the AO mirror in its place in the AOSLO as shown in Fig. 1, an additional optical setup was built. This is constituted by a He-Ne laser, a spatial filter, a collimating lens to generate an aberration-free beam and a set of flat mirrors to direct the light onto the DM and finally to the CCD, where the PSF is registered after being focused by a 100-mm focal length lens. The angle of incidence on the AO mirror was less than 2 degrees, the minimum achievable considering the space requirements. Through the maximum aperture of the AO mirror –3.5 mm- a sequence of three snapshots were taken and averaged to yield the final PSF.

The so obtained image is shown in Fig. 4. For comparison, together with the experimentally obtained PSF, the ideal PSF expected under the same conditions was calculated and is also shown on the same graph. The measured PSF (FWHM =  $31.2\ \mu\text{m}$ ) is very similar to the Airy disk (FWHM =  $18.7\ \mu\text{m}$ ), revealing the flatness of the AO mirror and the absence of relevant diffraction effects that could affect the AOSLO image quality. Only when the CCD is saturated is possible to reveal -see panel c)- the dimmest diffraction structure caused by the hexagonal segment arrangement.

##### 3.1.2. Double pass image evaluation

Another valuable element to assess the quality of the AO correction is the actual light intensity distribution on the confocal pinhole in the AOSLO which is the ultimate determination of the optical image quality. To the aim of registering this light distribution, the model eye was used together with a removable flat mirror placed between lenses L2 and L3 that directed the focusing light from L2 onto a CCD camera located at its focal plane. The light source used was the AOSLO's infrared laser (840 nm). The so obtained intensity distribution is the DPI through the AOSLO and model eye optics. This DPI can be easily rescaled to the actual light distribution on the pinhole simply considering the ratio between the focal length of lenses L1 and L2. Although there is a non-common path between lenses L1 and L2 both are doublets carefully aligned and the obtained DPIs will serve to the purpose of determining whether the optical performance is affected by diffraction or imperfections in the DM.

The DPIs obtained after correcting different amounts of defocus ( $-0.50\ \text{D}$ ,  $-0.25\ \text{D}$ ,  $+0.25\ \text{D}$ ,  $+0.50\ \text{D}$ ) induced by placing the corresponding trial lenses in front of the model eye were recorded. The procedure consisted of making the AO system correct for the aberrations

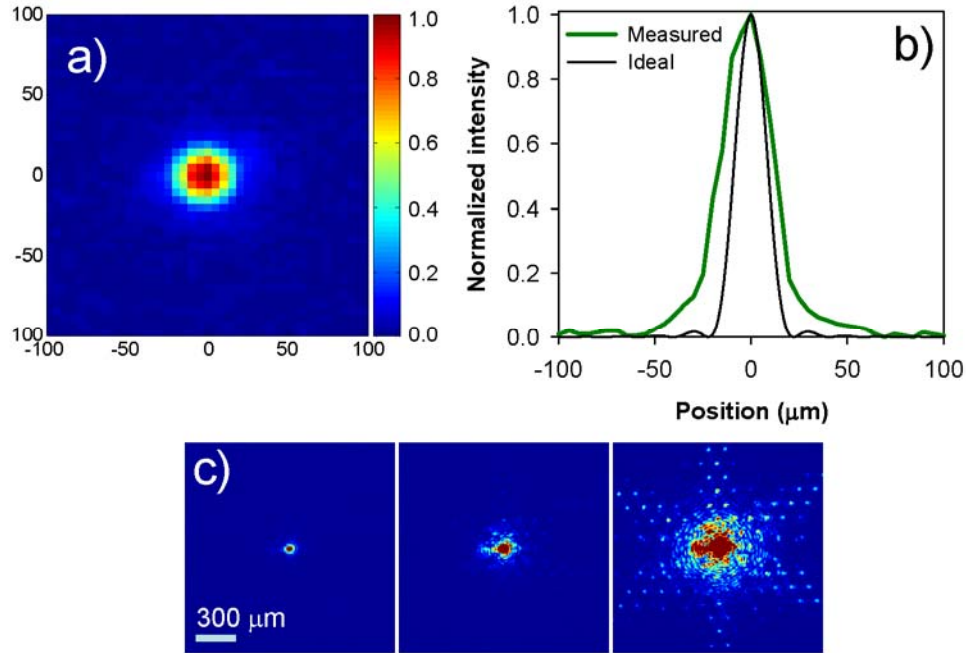


Fig. 4. a) PSF produced by the flat AO mirror. Pupil size is 3.5 mm, wavelength is 633 nm and the focal length of the focusing lens is 100 mm. The energy distribution is normalized to unity and the scale on x-y axis represents microns on the CCD. b) Measured energy distribution along the x-axis. For comparison, the theoretically expected PSF from a diffraction limited system, labeled as “ideal”, is also shown. c) Wide-field PSFs obtained saturating the CCD with increasing intensity from left to right to show the dimmest details.

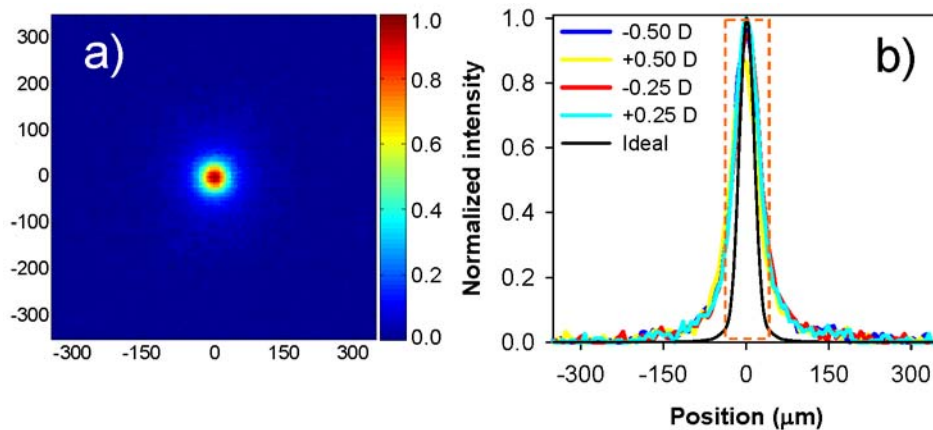


Fig. 5. a) DPI obtained after correcting + 0.25 D of defocus. The energy distribution is normalized to unity and the scale on the x-y axis represents microns on the pinhole plane. b) Energy distributions along the x-axis after correcting the different amounts of defocus. For comparison, the theoretically expected DPI from a diffraction limited system (autoconvolution of the Airy disk) is also shown. The dashed line rectangle indicates the relative size of the 80  $\mu\text{m}$  diameter pinhole employed as the confocal aperture. Wavelength is 840 nm, data are rescaled to a 100 mm focal length focusing lens and the beam diameter over this lens is 3.5 mm.

present in the optical system, then holding the AO mirror and placing the removable flat mirror in its location to record the DPI. To reduce noise, 10 images were averaged to yield the final DPI for each correction. Figure 5a shows the resulting DPI after correcting + 0.25 D of

defocus. For the rest of the defocus corrections the registered energy distribution along the x-axis was extracted from each final DPI for all the corrections (Fig. 5b). For comparison, the theoretically expected DPI from a diffraction limited system, computed as the autoconvolution of the Airy disk, is also shown on the same graph.

As expected from the PSF evaluation, the recorded DPIs (FWHM = 53.8  $\mu\text{m}$ ) are close to the ideal energy distribution (FWHM = 31.7  $\mu\text{m}$ ) under the same conditions and no significant diffraction effects are noticed. The DPI analysis also allows us to evaluate the optical performance not only for a flat AO mirror, as in the PSF evaluation case, but when the AO mirror is correcting for different amount of aberrations, which has a major practical interest. Figure 5 shows that all the DPIs are very similar through the range of tested defocus and there is only a slight decrease in the maximum intensity for the + 0.50 D case. From these results a uniform retinal image quality is expected when the AO system corrects for different amounts and types of aberrations.

### 3.1.3. Checking the flatness of the segments

For this particular AO mirror, another aspect to be considered in the evaluation of the AO correction is the performance in correcting defocus with opposite signs. If there is a high enough bow in the AO mirror segments [22] then this could lead to a better fit to defocused wavefronts with a certain sign. For example, concave segments would fit better to concave wavefronts, giving a better correction and better images. To determine if this particular AO mirror has similar effects, the model eye was used to obtain AOSLO images after correcting induced defocus from  $-0.50$  D to  $+0.50$  D in  $0.25$  D steps, using spherical trial lenses and a parallel lens for the  $0$  D case. The mean gray level in the image was chosen as a simple parameter to compare the AO correction quality through the different cases. The results are graphed in Fig. 6, showing that the mean gray level remains nearly constant and hence there is no different performance when correcting defocus with different signs. Although there is a slight decrease in the mean gray level at  $+0.50$  D, any bow in the segments is not likely to be responsible for it, since a difference would have been observed between  $-0.25$  D and  $+0.25$  D. Together with the mean gray level, the initial RMS and the final RMS achieved after each correction are also plotted. The symmetry of both graphs around  $0$  D shows that the equal image quality performance for positive and negative defocus is not biased neither by different initial requirements (Initial RMS) or different performance on the wavefront corrections (Final RMS).

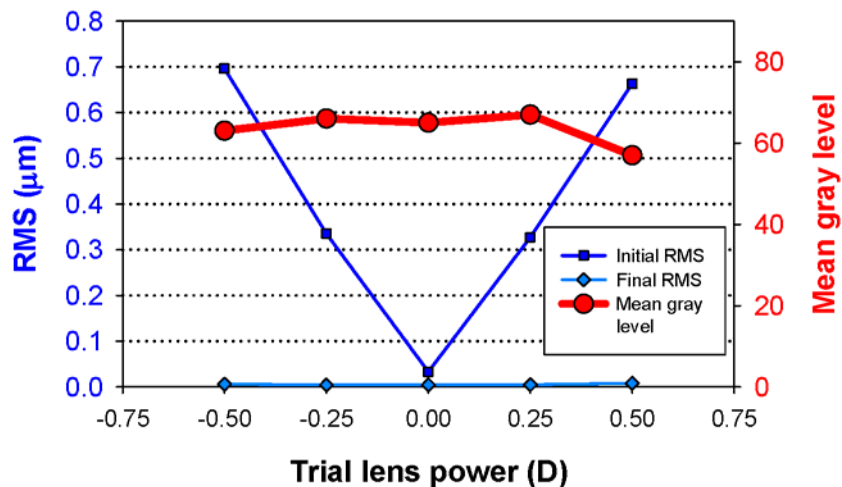


Fig. 6. Mean gray level (right y-axis) in the images recorded by the AOSLO after correcting different amounts of defocus induced by the corresponding trial lenses. On the left y-axis are represented the initial RMS before the AO correction and the final RMS achieved after the said correction.

### 3.2. AO performance on real eyes

Four different normal subjects, identified as A, B, C and D, were imaged in the AOSLO system. Prescriptions are  $-0.50$  DS,  $-1.75$  DS,  $-3.00$  DS and pl respectively. Research procedures adhered to the tenets of the Declaration of Helsinki. The study protocol was approved by the institutional review board of the University of California, Berkeley. All subjects gave written informed consent before participation in the studies. A 6.4 mm pupil was used, which made use of the entire AO mirror aperture. Subjects' eyes A and C were dilated using 0.5% tropicamide. Subject B had natural pupil large enough to fill the required pupil size and subject D, although his natural pupil was smaller than 6.4 mm, it was considered large enough to allow retinal imaging and his pupil was not artificially dilated. The wavelength was 840 nm and the power employed to illuminate the retina was about  $210 \mu\text{W}$  at the eye pupil plane.  $0.9^\circ \times 0.9^\circ$  field of view images were acquired from retinal locations at the foveal center (Fig. 7) and  $1^\circ$  temporal (Fig. 8). Raw videos were corrected for scanning distortions and distortions caused by eye motions and then all stabilized frames were averaged to generate high signal-to-noise images [39]. For all the subjects the acquired images showed resolved retinal features at the cellular level with the typical inter-subject variability that is

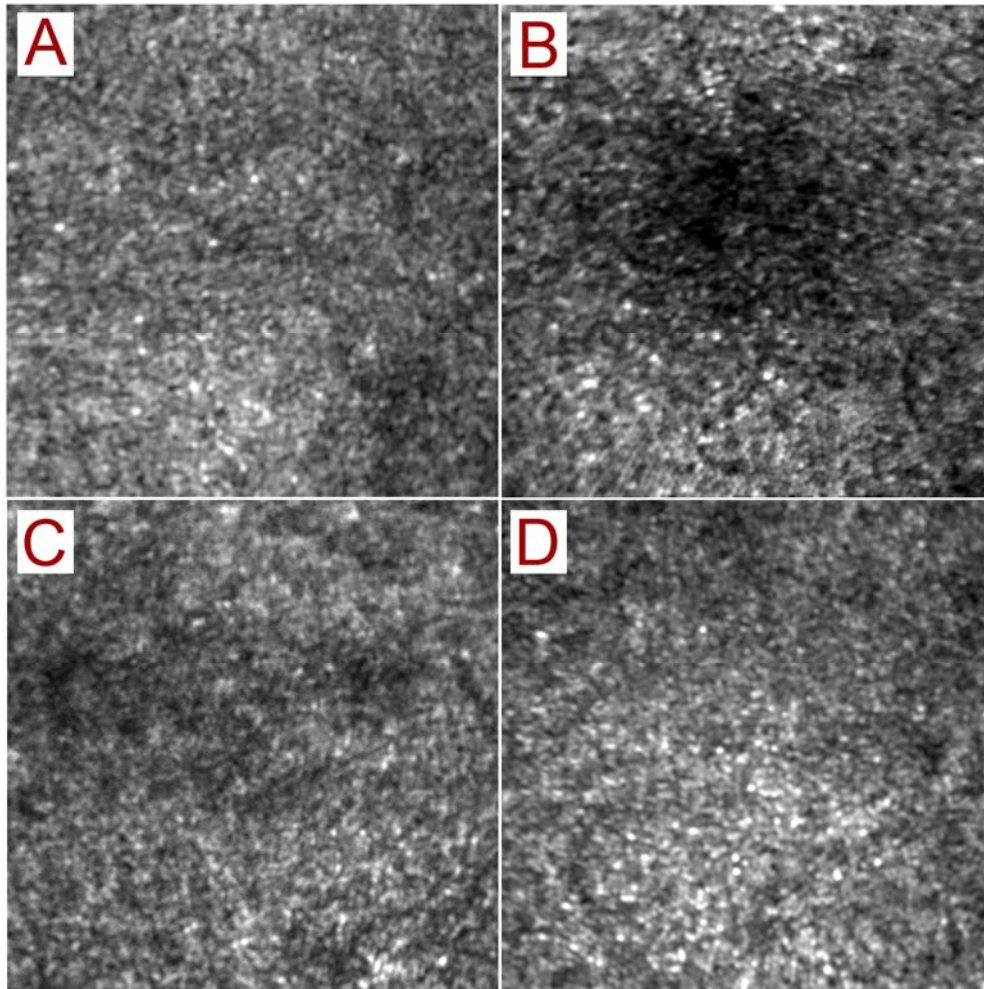


Fig. 7. Retinal images taken at the central fovea obtained from subjects A, B, C and D. The field of view is  $0.9^\circ \times 0.9^\circ$ .

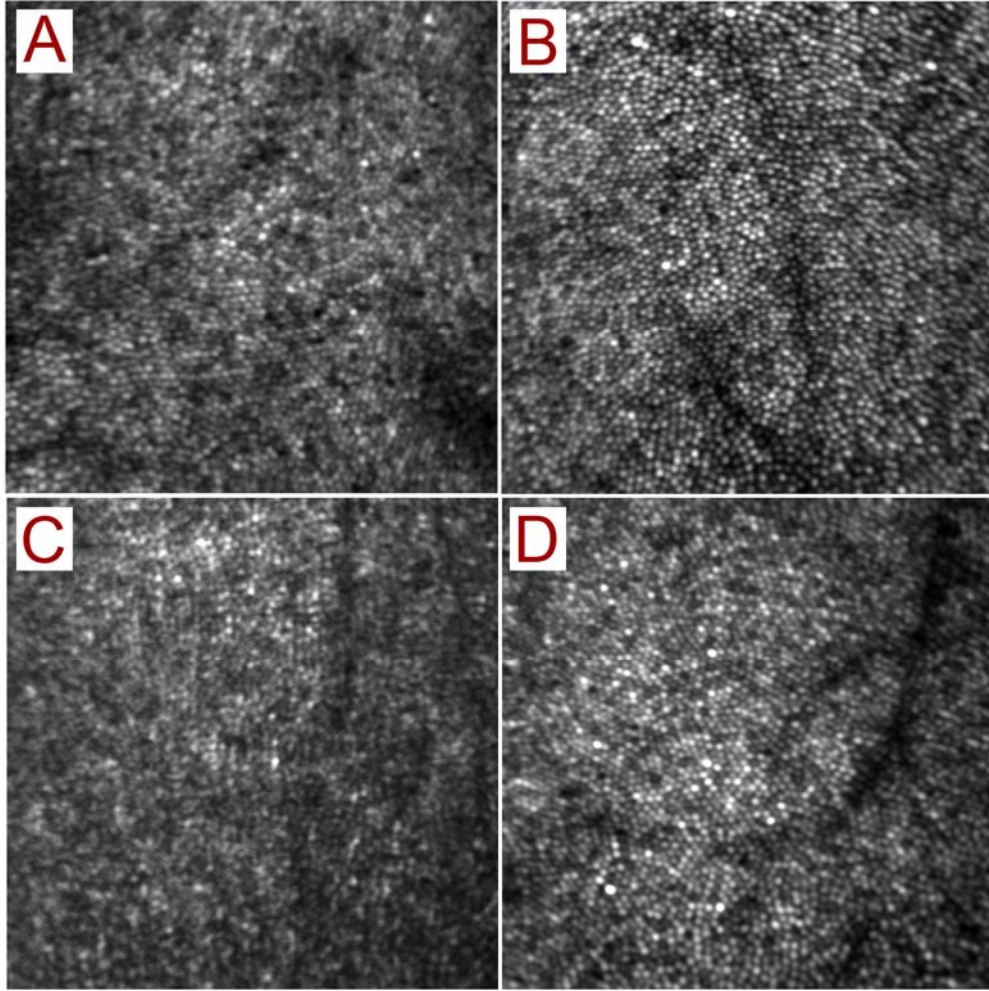


Fig. 8. Retinal images taken at  $1^\circ$  temporal obtained from subjects A, B, C and D. The field of view is  $0.9^\circ \times 0.9^\circ$ .

experienced with other AOSLOs that make use of different AO technologies. The best images were obtained from subject B, where it is possible to discern cone photoreceptors at  $0.25^\circ$  from the foveal center.

To obtain the retinal images shown in both figures, we made use of the tools -described in the methods section- available in the AO control, in particular the possibility of selecting the pupil size that is used to estimate the aberrations on the whole pupil (6.4 mm). Starting with the largest possible pupil we switched to a smaller one when the AO control was not able to provide high quality images. For subject A the AO correction was performed making use of the wavefront sampling provided by the inner 19 lenslets (4.6 mm diameter sensing region). For subjects C and D the inner 31 lenslets (5.9 mm diam.) were used. And for subject B the best images were acquired when all the 37 lenslets (6.4 mm diam.) were employed. Independently of the sensing region used to estimate the complete wavefront, the retinal images were always obtained through the 6.4 mm pupil, except for subject D whose pupil was not big enough to fill the maximum aperture.

Figure 9 plots the performance of the AO system, showing the obtained RMS considering up to 5th order Zernike terms, before and after the AO correction on each of the 4 subjects. Six different AO corrections were carried out on each subject, and the last 151 measurements

(2.5 s) after the closed-loop was stable, were averaged. These 6 mean values were, in turn, averaged and their standard deviation calculated to yield the final value and error bars respectively. Note that in this case error bars do not represent the stability through the closed-loop operation, but the stability through different AO corrections. The same applies for the RMS measured before initiating the closed-loop. As can be observed in Fig. 9, in all subjects the final RMS was always below 0.11  $\mu\text{m}$ . It should be remarked that these RMS data were obtained for a 6.4 mm pupil, independently of the sensing region that was actually used to estimate the wavefront correction that was applied to the DM.

The initial RMS was measured after correcting defocus and astigmatism by means of trial lenses placed in front of the eye to mitigate against the stroke limits of the AO mirror.

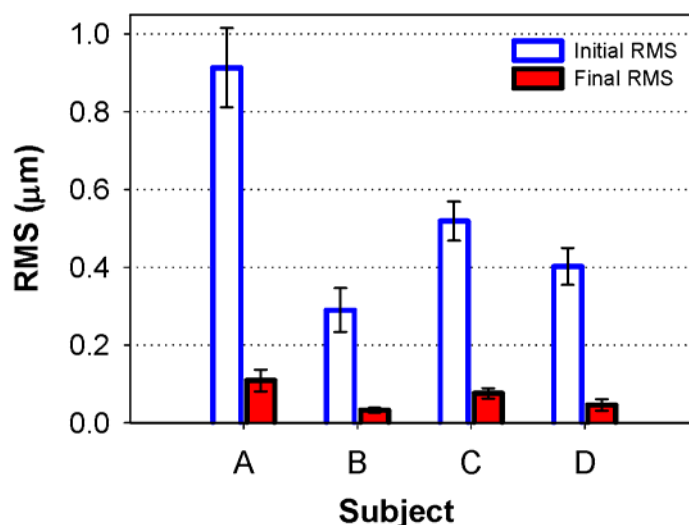


Fig. 9. AO performance for subjects A, B, C and D. The initial RMS wavefront error is measured before the AO correction but after correcting defocus and astigmatism with trial lenses. The final RMS is measured after the AO correction. RMS is computed using up to 5th order Zernike terms. Six measurements were used to obtain the RMS values and their error bars, which represent  $\pm 1\text{SD}$ . (See text for details). Pupil size is 6.4 mm.

In order to understand the AO correction performance in more detail, Fig. 10 shows plots of the Zernike coefficient values that fit the measured wavefront errors for the six AO corrections performed on each subject and that were used to compute the RMS values graphed on Fig. 9. The procedure followed to obtain the final values and the significance of their corresponding error bars is the same as that of the RMS values. Figure 10 shows that the AO control system provided an excellent correction over those Zernike terms it was asked to correct. The corresponding bars on the graph are so small that they are not distinguishable and those terms averaged almost to zero (some noise may have remained but is not revealed in this plot due to the averaging method employed). In addition, the equally negligible error bars indicate that this final correction state was very stable through the different closed-loop operations performed.

#### 4. Discussion

We do not claim that the images presented in this paper represent the best possible performance of an AO ophthalmoscope (see Rossi et al. [29], for the best examples). But it is important to note that these images were obtained with a modest number of actuators and using a Shack-Hartmann WFS with a limited number of lenslets (37) to sample the wavefront. Although 37 lenslets should be high enough to correct the most important aberrations in the general population [40], the numbers shown in Fig. 9 and Fig. 10 do not imply that perfectly

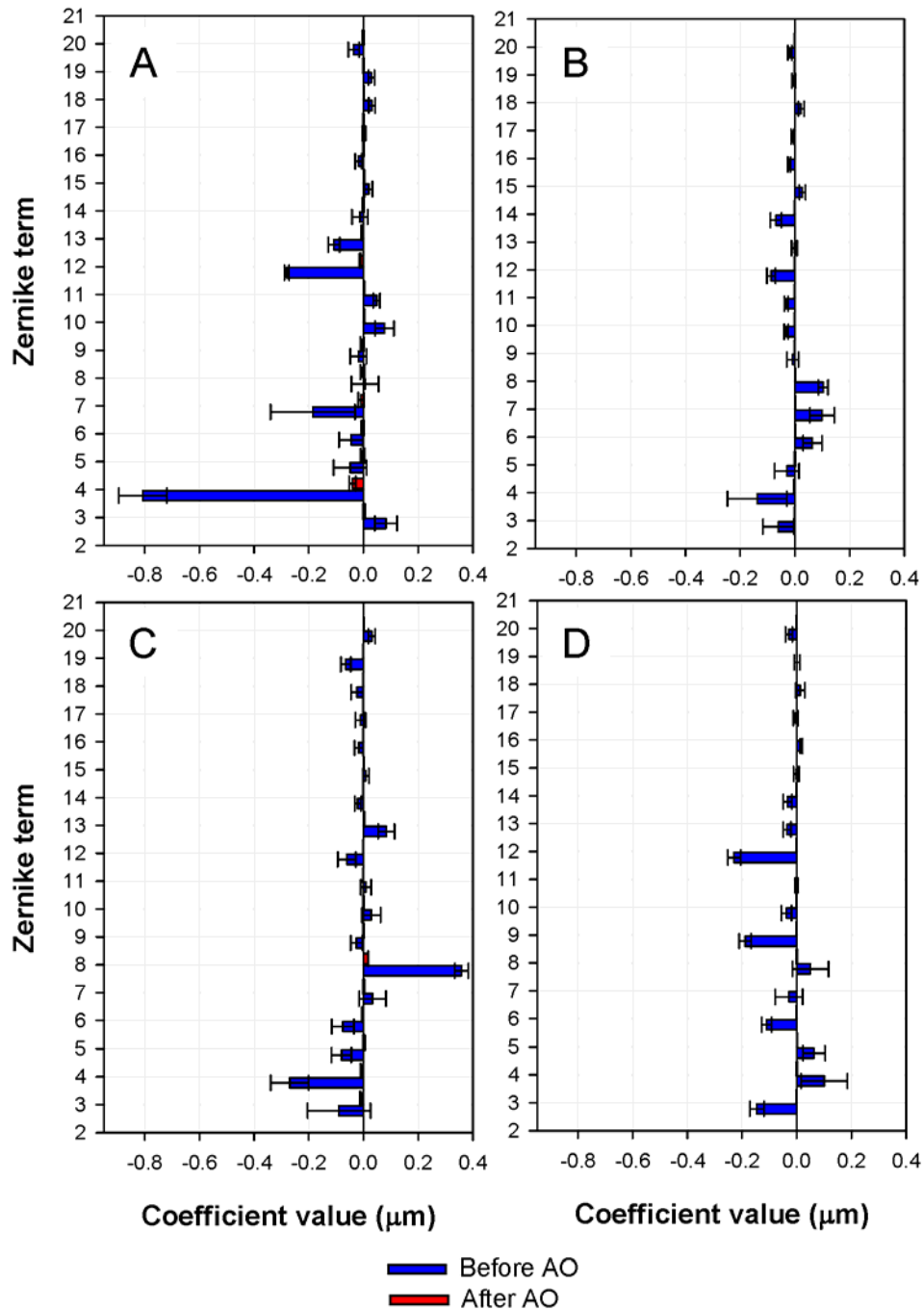


Fig. 10. Wavefront error in terms of Zernike polynomials up to 5th order measured before and after AO correction for subjects A, B, C and D. Values are the average through 6 different measurements and error bars represent  $\pm 1$ SD (see text for further details). Pupil size is 6.4 mm.

error-free wavefronts were achieved. Moreover, the AO correction seems to perform equally well in both, higher and lower order terms, which is unexpected considering that the AO corrector utilizes only 37 segments. Therefore, what actually can be claimed from Fig. 10 is

that the AO control system performs quite well correcting those aberrations that is able to detect.

One of the most important concerns when employing segmented mirrors is the presence of undesired diffraction effects. This is particularly important in retinal imaging where the size and quality of the PSF determines the achievable image resolution. But with a 98% fill factor and carefully cophased segments, the AO mirror tested in this work has shown, under the performed test, to be relatively free of these effects.

## **5. Conclusions**

A MEMS segmented AO mirror (37 segments) has been used as the aberration corrector in an AOSLO to evaluate the capabilities and potential of this type of technology in vision systems.

Some tests using a model eye were initially performed. They showed: i) that the flatness of the segments in the mirror was high enough to not affect the AO performance in the sense that the same image quality is obtained correcting positive or negative defocus and ii), that neither the PSF recorded from a flat AO mirror nor the DPIs registered after correcting different amounts of defocus showed unwanted diffraction effects from the segments.

Retinal images located at the fovea and 1° temporal were acquired from 4 normal subjects. The AO correction yielded a wavefront error (sampled by 37 lenslets) always below 0.11 μm and, despite the moderate number of segments in the AO mirror, cone photoreceptors were imaged as close as 0.25° from the foveal center in one of the subjects. It is possible, considering the normal inter-subject variability, to acquire retinal images with similar quality to that obtained with AOSLOs that make use of AO mirrors based on different technologies.

## **Acknowledgments**

This work has been funded by Ministerio de Educación y Ciencia, Human Resources Mobility National Program I-D + I 2008-2011 (Spain), National Science Foundation grant NSF AST 9876783 and National Institutes of Health grant NIH EY14735.